Two-dimensional multiferroics in monolayer group IV monochalcogenides

2017 2D Mater. 4 015042

(http://iopscience.iop.org/2053-1583/4/1/015042)

2D Materials

RECEIVED
25 August 2016

REVISED
9 November 2016

ACCEPTED FOR PUBLICATION
21 November 2016

PUBLISHED
13 January 2017

PAPER

Two-dimensional multiferroics in monolayer group IV monochalcogenides

Hua Wang and Xiaofeng Qian

Department of Materials Science and Engineering, College of Engineering and College of Science, Texas A&M University, College Station, Texas 77843, USA

E-mail: feng@tamu.edu

Keywords: two dimensional materials, 2D multiferroics, optoelectronic properties, domain wall physics, first-principles calculations

Supplementary material for this article is available online

Abstract

Low-dimensional multiferroic materials hold great promises in miniaturized device applications such as nanoscale transducers, actuators, sensors, photovoltaics, and nonvolatile memories. Here, using first-principles theory we predict that two-dimensional (2D) monolayer group IV monochalcogenides including GeS, GeSe, SnS, and SnSe are a class of 2D semiconducting multiferroics with giant strongly-coupled in-plane spontaneous ferroelectric polarization and spontaneous ferroelastic lattice strain that are thermodynamically stable at room temperature and beyond, and can be effectively modulated by elastic strain engineering. Their optical absorption spectra exhibit strong in-plane anisotropy with visible-spectrum excitonic gaps and sizable exciton binding energies, rendering the unique characteristics of low-dimensional semiconductors. More importantly, the predicted low domain wall energy and small migration barrier together with the coupled multiferroic order and anisotropic electronic structures suggest their great potentials for tunable multiferroic functional devices by manipulating external electrical, mechanical, and optical field to control the internal responses, and enable the development of four device concepts including 2D ferroelectric memory, 2D ferroelastic memory, and 2D ferroelastoelectric nonvolatile photonic memory as well as 2D ferroelectric excitonic photovoltaics.

1. Introduction

The last decade has witnessed tremendous progress in two-dimensional (2D) materials [1–6] research, leading to the remarkable discoveries of 2D metals, semiconductors, and insulators and, equally important, a variety of rich physics such as massless [3] and massive Dirac fermions [7] and topological insulators [8, 9]. Recently, coupled physical properties of 2D materials attract a lot of attention for their potentials device and energy applications. For example, monolayer BN [10], MoS_2 [11–13] and group IV monochalcogenides [14, 15] were recently found to possess large piezoelectricity [17] which allows efficient mechanical-to-electrical energy conversion. Monolayer $CrSiTe_3$ was experimentally synthesized and demonstrated with 2D ferromagnetic ordering [16, 18], paving the way towards 2D spintronics. Interestingly, Peierls-distorted 1T' transition metal chalcogenide have been predicted to exhibit both quantum spin Hall effect with a nontrivial Z_2 topological index [19, 20] and ferroelasticity [21], suggesting the possibility of controlling the anisotropy of the topologically-protected edge states via elastic strain engineering [22].

The 2D materials mentioned above possess one ferroic order only. Undoubtedly, 2D multiferroic materials that hold simultaneously two or more primary ferroic (i.e., ferroelectric, ferromagnetic, and ferroelastics) orders are highly desirable as they will open up unprecedented opportunities for both scientific and technological endeavors [23–29]. Ideal multiferroics, however, require different order parameters to be strongly coupled, which in tandem with appropriate kinetic barrier of phase transition will allow facile switching of electric polarization, magnetization, and lattice strain through external disparate fields. Though highly valuable, perfect multiferroic

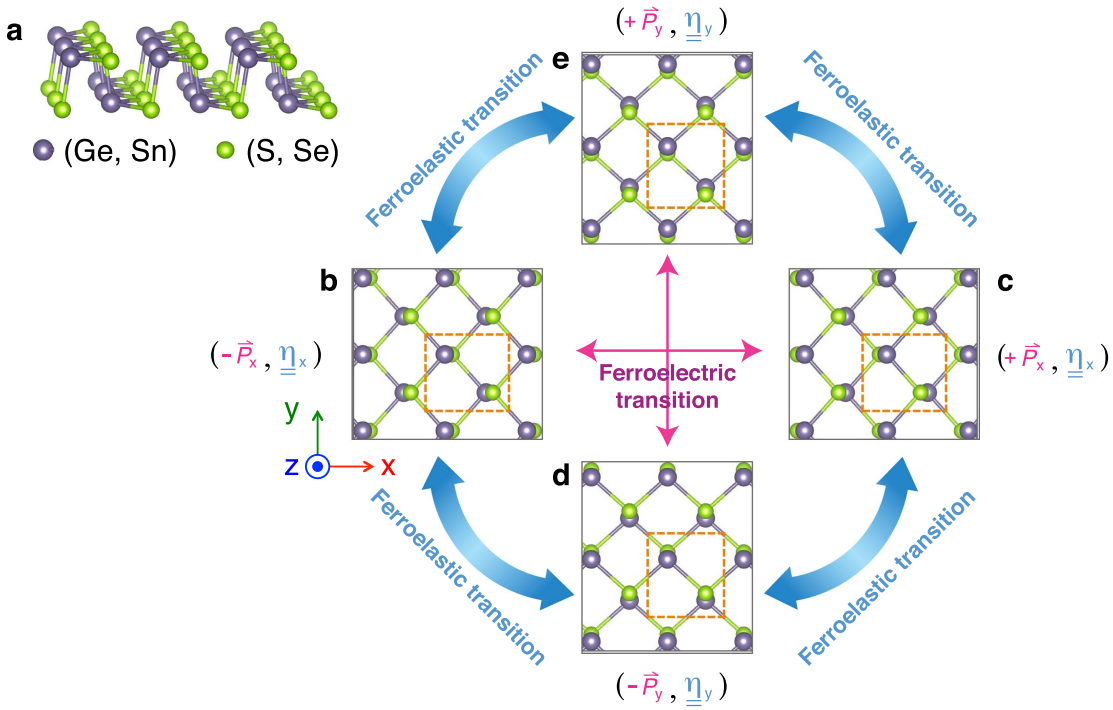

Figure 1. Structure of monolayer group IV monochalcogenides (MX) and their ferroelastic and ferroelectric orders. (a) Perspective view of free-standing MX monolayer using GeSe as an example. (b) and (c): two ferroelectric states with opposite spontaneous polarization along the x axis: $-P_x$ and $+P_x$. (d) and (e): two ferroelectric states with opposite spontaneous polarization along the y axis: $-P_y$ and $+P_y$. (b)–(e): two ferroelastic states with spontaneous tensile strain along x and y relative to the centrosymmetric paraelastic structure. The corresponding transformation strain matrices are denoted by $\boldsymbol{\eta}_x$ and $\boldsymbol{\eta}_y$.

materials especially in low dimensions are scarce, largely due to the stringent symmetry and chemistry requirements for the coexistence of two or more coupled ferroic orders and good thermodynamic stability for practical applications at room temperature [23, 27].

Based on first-principles theory, here we predict that monolayer group IV monochalcogenides (including GeS, GeSe, SnS, and SnSe) represent a class of 2D multiferroic materials that simultaneously possess strongly-coupled ferroelectric and ferroelastic orders and, more importantly, have low domain wall energy and small migration barrier. The calculated giant intrinsic in-plane electric polarization implies that their thickness is not constrained by out-of-plane depolarization-induced instability that often occurs in free-standing multiferroic ultrathin films [30]. As ferroelastic order in these monolayers is pertinent to spontaneous strain of unit cell along two perpendicular orientations, the direct coupling between ferroelastic lattice strain and ferroelectric polarization allows the direct control of one ferroic order by applying external field that is conjugated with the other one. Furthermore, the spontaneous lattice strain and in-plane polarization also lead to highly anisotropic electronic and optical properties. Therefore, these 2D ferroelastoelectric semiconducting monolayers with highly anisotropic, strongly coupled, and externally switchable physical properties will engender a wide variety of ultrathin mechano-opto-electronic applications. Applications of elastic strain, electric field, or optical field can efficiently switch the multiferroic states and alter their electric, optical, and mechanical responses, thereby enabling the conceptual designs of 2D ferroelectric, ferroelastic, and ferroelastoelectric nonvolatile photonic memories as well as 2D ferroelectric excitonic photovoltaics presented below.

2. Ferroelastic order and spontaneous strain in monolayer MX

Monolayer group IV monochalcogenide (abbreviated as MX), as shown in figure 1(a), consists of two puckered atomic layers similar to monolayer black phosphorus where M = (Ge, Sn) and X = (S, Se). We use GeSe as an example and set the x-axis and y-axis as in-plane axes with the z-axis along the plane normal. Its noncentrosymmetric unit cell is illustrated by dashed orange rectangle in figures 1(b)–(e), which contains four atoms and belongs to space group $Pmn2_1$ with a mirror symmetry only (M_y: $y \rightarrow -y$). The lattice parameters are optimized by first-principles density functional theory (DFT) [31, 32] calculations (listed in supplementary materials), in good agreement with other theoretical results [14, 33–35]. Figures 1(b)–(e) show the corresponding ferroelectric phase with spontaneous polarization along $-x/+x$ and $-y/+y$, respectively, while a direct comparison of

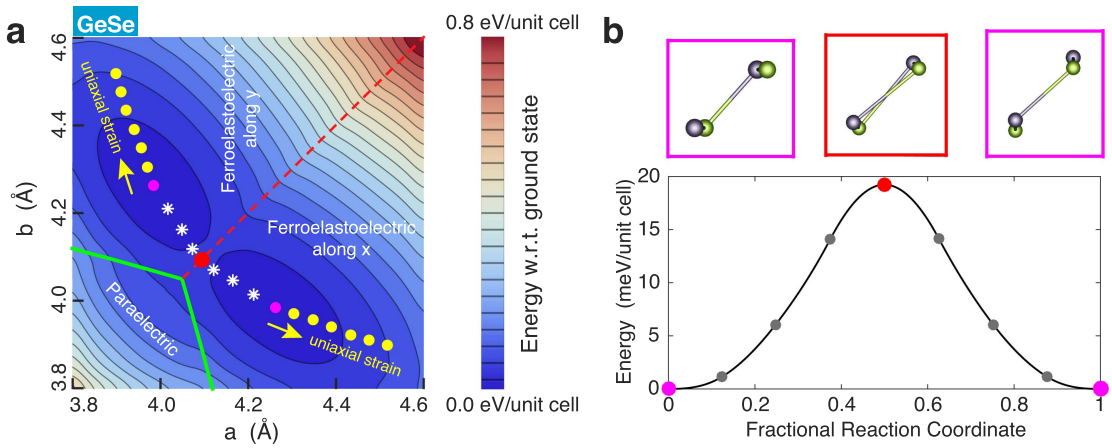

Figure 2. Ferroelastic order and spontaneous strain in monolayer GeSe. (a) Total energy of monolayer GeSe with different lattice parameters a and b with respect to their ferroelectric ground state. Solid green line: phase boundary between paraelectric and ferroelectric phases. Red dashed line: phase boundary between two ferroelastoelectric phases with spontaneous strain along x and y, respectively, where ferroelectric polarization will be along $+x/-x$ and $+y/-y$, respectively. Two purple dots stand for the two ferroelastoelectric ground states at stress-free condition, while the yellow dots stand for the corresponding lattice parameters upon uniaxial tensile strain along x and y axis. The contour colors illustrate the total energy of unit cell relative to the energy of ferroelectric ground states (purple dots). (b) Minimum energy pathway of coherent ferroelastic transition. The gray dots in (b) correspond to the white stars in (a).

figures 1(b)–(e) reveals the ferroelastic order with spontaneous strain along x and y, respectively. Below we will separately discuss the ferroelastic and ferroelectric order in monolayer MX.

Ferroelastic order in MX monolayers originates from the fact that their centrosymmetric parent phase can undergo spontaneous relaxation along both x and y direction, resulting in two different orientations of spontaneous lattice strain that are perpendicular to each other. For 2D materials, it can be mathematically described by 2×2 in-pane transformation strain matrix using the paraelastic structure as a reference state. For one of the two ferroelastic ground states of monolayer GeSe with spontaneous tensile strain along x, the lattice parameters a and b are 4.26 and 3.98 Å, respectively, which are 4.10 and 4.10 Å in the reference paraelastic phase. According to its space group $Pmn2_1$, two in-plane lattice vectors are perpendicular to each other. Hence, the corresponding 2×2 in-plane unit cells $\mathbf{H}_x$ and $\mathbf{H}_{\mathrm{ref}}$ can be expressed by: $\mathbf{H}_x = \begin{bmatrix} 4.26 & 0 \\ 0 & 3.98 \end{bmatrix}$ and $\mathbf{H}_{\mathrm{ref}} = \begin{bmatrix} 4.10 & 0 \\ 0 & 4.10 \end{bmatrix}$. Transformation strain matrix $\boldsymbol{\eta}_x$ can be defined using the Green-Lagrange strain tensor, $\boldsymbol{\eta}_x = \frac{1}{2}([\mathbf{H}_{\mathrm{ref}}^{-1}]^{\mathrm{T}}\mathbf{H}_x^{\mathrm{T}}\mathbf{H}_x\mathbf{H}_{\mathrm{ref}}^{-1} - \mathbf{I})$ [21], where $\mathbf{T}$ denotes matrix transpose, and $\mathbf{I}$ is a 2×2 identity matrix. For GeSe, $\boldsymbol{\eta}_x = \begin{bmatrix} 0.041 & 0 \\ 0 & -0.027 \end{bmatrix}$, corresponding to 4.1% tensile strain along x and 2.7% compressive strain along y. Similarly, we obtained transformation strain matrix $\boldsymbol{\eta}_y$ for the other ferroelastic ground state: $\boldsymbol{\eta}_y = \begin{bmatrix} -0.027 & 0 \\ 0 & 0.041 \end{bmatrix}$, indicating a 2.7% compressive strain along x and 4.1% tensile strain along y. The results for other materials can be found in the supplementary materials.

To have a better physical picture of the ferroelastic order, we calculate the total energy of fully relaxed monolayer GeSe as function of lattice parameters a and b with respect to the ground-state state energy. The results are shown in figure 2(a). Two degenerate ground states are marked by two purple dots characterized by spontaneous strain along x and y, respectively. Under relatively large in-plane lattice parameters, two ferroelastic phases are separated by a phase boundary, whereas at smaller lattice parameters they undergo a ferroelectric-to-paraelectric transition. Furthermore, a generalized solid-state nudged elastic band (NEB) calculation [36, 37] was performed to investigate the coherent structural transition from one ferroelastic state to the other. The calculated minimum energy pathway (MEP) is shown in figure 2(b) and marked by white stars in figure 2(a), and the saddle point is labeled by red dot. The small energy barrier of 19 meV/unit cell in monolayer GeSe highlights the possibility of fast switching upon external mechanical stress despite the fact that such switching is generally mediated by domain wall motion. It is worthy to note that the ferroelastic transition does not go through the centrosymmetric paraelectric phase where Ge and Se atoms overlap exactly in the 2D plane. Instead, as shown in figure 2(b), the Ge and Se atoms rotate around each other.

3. Ferroelectric order and spontaneous polarization in monolayer MX

Ferroelastic order does not necessarily correlate with ferroelectric order. Monolayer black phosphorus is a good example which shares a similar structure with monolayer MX, hence it is a 2D ferroelastic material

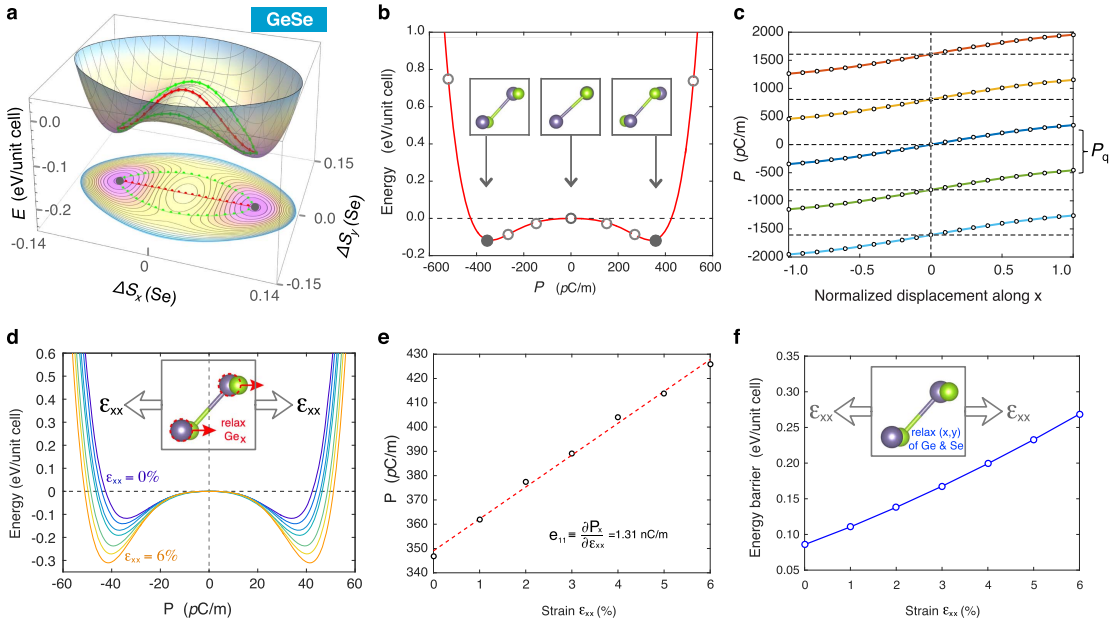

Figure 3. Ferroelectric order, spontaneous polarization, and elastic strain effect in monolayer GeSe. (a) Potential energy surface with fractional shift of Se atoms along x and y with the fixed ground-state lattice parameters. Green lines: MEP for ferroelectric transition. Red line: adiabatic path for polarization calculation. Two black dots: degenerate ferroelectric ground states. (b) Double-well potential of monolayer GeSe along the adiabatic path. (c) Calculated total polarization as a function of normalized displacement where the centrosymmetric paraelectric phase (0% displacement) is at the center, and two ferroelectric ground states are at two ends. P_q represents the polarization quanta. (d) Effect of uniaxial strain on the total energy and total spontaneous polarization. (e) Spontaneous polarization of ferroelectric GeSe monolayer as function of uniaxial strain. (f) Minimum energy barrier of coherent ferroelectric transition as function of uniaxial strain without the constraint through the paraelectric phase.

[38]. Nonetheless, due to single phosphorus element no ferroelectric order is expected. In contrast, the two distinct chemical elements in monolayer MX give rise to appreciable difference in electronegativity and large relative displacement, consequently they are very likely to have large spontaneous polarization. To confirm the above speculation, we need to choose an adiabatic pathway for the ferroelectric transition, and calculate its spontaneous polarization using the Berry phase approach based on the Kohn-Sham wavefunctions from first-principles DFT calculations. First, we scanned the full potential energy surface by fixing the Ge atoms in the unit cell, shifting Se atoms with respect to their hypothetic centrosymmetric position in the x-y plane, and then relaxing the atoms along the z-axis. Here, the lattice parameters are constrained to the initial ground state, and the centrosymmetric phase serves as the reference point of total energy. Figure 3(a) clearly shows that two ferroelectric ground states are located at the minima of two potential energy wells. Our NEB calculations show that these two energy minima are connected by two MEPs (marked with green lines) which deviate away from the central paraelectric phase, implying that bulk ferroelectric transition is realized by the relative rotation of Ge and Se atoms around their paraelectric positions, rather than by a straight translation between two ferroelectric phases (marked as red line). The calculated minimum energy barrier for monolayer MXs spans a wide range, i.e. about 7, 33, 95, and 464 meV/unit cell for SnSe, SnS, GeSe, and GeS, respectively, suggesting a possibility to fine-tune the kinetic barriers of ferroelectric transition via stoichiometric controls of M and X chemical elements for device applications.

The adiabatic path through MX's centrosymmetric paraelectric phase allows us to calculate the total polarization using modern theory of polarization based on the Berry phase approach [39, 40]. Mathematical expression of spontaneous polarization P_s in Wannier representation is given by

$$P_s = P^{\mathrm{f}} - P^{\mathrm{i}} = \frac{1}{\Omega}\sum_j (q^{\mathrm{f}}\mathbf{r}^{\mathrm{f}} - q^{\mathrm{i}}\mathbf{r}^{\mathrm{i}}) - \frac{2ie}{(2\pi)^3}\sum_n^{\mathrm{occ}}\left[\int_{\mathrm{BZ}} d^3\mathbf{k}\, e^{-i\mathbf{k}\cdot\mathbf{R}} \times \left\langle u^{\mathrm{f}}_{n\mathbf{k}} \left| \frac{\partial u^{\mathrm{f}}_{n\mathbf{k}}}{\partial \mathbf{k}} \right\rangle - \left\langle u^{\mathrm{i}}_{n\mathbf{k}} \left| \frac{\partial u^{\mathrm{i}}_{n\mathbf{k}}}{\partial \mathbf{k}} \right\rangle \right.\right],$$

where 'i' and 'f' refer to the initial and final positions, and $u_{n\mathbf{k}}(\mathbf{r})$ is the periodic part of Bloch wave functions $u_{n\mathbf{k}}(\mathbf{r}) = e^{-i\mathbf{k}\cdot\mathbf{r}}\psi_{n\mathbf{k}}(\mathbf{r})$, Ω is the volume of the unit cell, and the integral is performed over the first Brillouin zone. Here, the initial state is the centrosymmetric structure, and the final state is the polarized one. The above formula has taken into account both ionic and electronic contributions to the total polarization. As shown in figures 3(b) and (c), monolayer GeSe has a large spontaneous polarization of 357.0 pC/m, rendering an effective bulk polarization of 35.7 μC/cm^2 if we assume an approximate layer thickness of 1 nm. The latter includes both van der

Waals distance and the intrinsic thickness of monolayer GeSe. Here, the spontaneous polarization was rigorously determined by identifying the continuous evolution of total polarization as a function of normalized displacement through the centrosymmetric paraelectric state, as shown in figure 3(c) for monolayer GeSe. The similar plots for the other three materials can be found in supplementary figure S1, and the lines with different colors in figure 3(c) are shifted by multiple polarization quanta P_q. Spontaneous polarizations for GeS, SnS, and SnSe monolayers are 484, 260, and 181 pC/m, respectively, corresponding to effective polarization of 48.4, 26.0, and 18.1 μC/cm^2, which agrees well with a very recent work by Fei *et al* [41] Monolayer GeS owns the largest spontaneous polarization owing to a sizable electronegativity difference of the two elements and, more importantly, the largest displacement between Ge and S atoms with respect to the paraelectric state.

Furthermore, as shown in figure 3(b), the total energy as function of spontaneous polarization along the adiabatic path (the red line in figure 3(a)) exhibits a characteristic double-well potential of ferroelectrics. The solid curve in figure 3(b) is obtained by fitting the energy as function of polarization in a sixth-order polynomial based on the Landau-Devonshire theory of ferroelectrics [42], $E(P) = \frac{1}{2}aP^2 + \frac{1}{4}bP^4 + \frac{1}{6}cP^6$, where E is the total energy with respect to the paraelectric phase and P is the total polarization. By including the energy contribution from the conjugate external electric field $\mathcal{E}$ and internal polarization, one can define electric enthalpy $F = E - \mathcal{E}P$, from which we can estimate the ideal coercive field $\mathcal{E}_c$ from the maximum slope of $E(P)$, i.e. $\mathcal{E}_c = \max\left(\frac{dE}{dP}\right)$, between the minimum and saddle point [29]. The calculated ideal coercive field $\mathcal{E}_c$ for monolayer GeSe is 0.623 V nm^{-1} under stress-free condition, which increases with increasing uniaxial strain along the polarization direction. However, two issues need to be kept in mind. First, the fitted *E-P* curve serves as a guidance only, as in principle the fitting parameters a, b, and c are temperature dependent which is not reflected in the present DFT calculations carried out at 0 K. Second, ideal coercive field $\mathcal{E}_c$ refers to the electric field required to reverse the polarization in a coherent transformation throughout the whole crystal, while in reality true coercive field corresponds to critical electric field that destabilizes the domain walls, which is often much smaller than the ideal coercive field $\mathcal{E}_c$.

2D materials can often sustain large elastic strain [43, 44], making it distinctly different from their 3D bulk counterpart. Specifically, the dual ferroic (ferroelastic and ferroelectric) properties in MX monolayers may be subject to continuous alternations upon elastic stress, which may offer a facile control of charge polarization and phase transition barrier and thus provide a broader design space for optoelectronic devices. To verify this concept, we apply a uniaxial tensile strain along x-axis (*i.e.* ferroelectric direction) and fully relax the lattice parameter b and the atomic positions. The resulted strain-dependent energy profile as function of total polarization is presented in figure 3(d) for monolayer GeSe, manifesting a large effect of elastic strain on the spontaneous polarization. For example, by increasing uniaxial strain from 0% to 6%, the spontaneous polarization in monolayer GeSe is markedly enhanced from 357 pC/m to 430 pC/m. The strain-dependent polarization as shown in figure 3(e) also allows us to estimate the piezoelectric coefficient $e_{11} \equiv \frac{\partial P_x}{\partial \epsilon_{xx}}$ of 1.31 nC/m for monolayer GeSe, which is in good agreement with the recent work by Fei *et al* [14]. Furthermore, as shown in figure 3(f), the strain-dependent coherent ferroelectric transition energy barrier enlarges from 0.08 to 0.30 eV/unit cell as strain increases from 0% to 6% (supplementary figure S2). The above results unequivocally demonstrate that elastic strain can have significant impact on both spontaneous polarization and coherent transition barriers, highlighting strain modulation as a potential avenue for fine-tuning ferroelectric properties of materials. To verify the stability of multiferroicity under room temperature, we have performed ab initio molecular dynamics (AIMD) simulations for monolayer GeSe at 300 K using NPT ensemble at zero pressure and a time step of 0.5 fs. Three configurations at t = 0, 900 fs, and 1800 fs are shown in supplementary figure S8. These snapshots of AIMD configurations demonstrate that the multiferroicity is preserved along the initial vertical direction after 1800 fs. However, it should be noted that the limited AIMD simulations cannot tell the absolute stability and the exact transition temperature of multiferroicity. Moreover, we cannot simply use the energetic difference between ground-state ferroelectric phase and paraelectric phase to determine the transition temperature. Instead, one has to apply the fourth order Landau theory to estimate transition temperature for ferroelectric crystals. This was also pointed out by Fei *et al* recently and they applied Monte Carlo simulations with an effective Hamiltonian method and demonstrated robust ferroelectricity in four MX materials beyond room temperature [41]. However, the Curie temperature of the multiferroic transition is more complicated than ferroelectric transition as Curie temperature depends on the mechanical boundary condition and one has to include the coupling of the two order parameters (ferroelectric and ferroelastic). This problem can be addressed using the phase-field approach [45] which can provide a quantitative prediction of both the transition temperature and the domain structure at a given temperature under a stress-free condition. However, this approach will involve substantial development that is beyond the scope of the current work, and is currently under investigation.

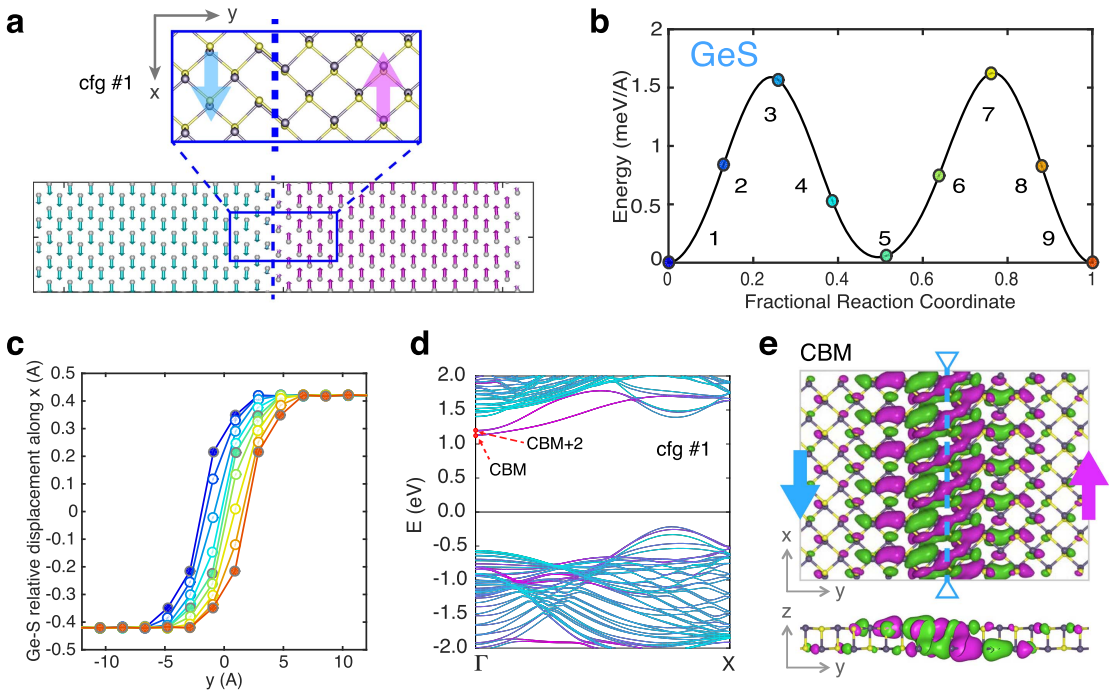

Figure 4. Ferroelectric domain wall in monolayer GeS. (a) Ground-state atomistic structure of 180° domain wall. Blue and purple arrows illustrate the polarization direction on the left-hand and right-hand side of the domain wall. (b) MEP of domain wall motion with initial, intermediate, and final configurations labeled from 1 to 9. (c) Relative displacement of each local Ge-S pair along the x direction. Colors from blue to red correspond to the configurations #1–#9 marked in (b). (d) Band structure of monolayer GeS supercell with 180° ferroelectric domain wall. Color indicates the relative localization of electronic states around the domain wall. (e) Top and side view of Kohn-Sham wavefunction at the conduction band minimum (CBM). Purple and green isosurfaces represent the positive and negative values of wavefunctions, respectively.

4. Ferroelectric domain wall in monolayer MX

The potential energy surfaces shown above illustrate only the thermodynamic properties of perfect crystalline monolayer MX, whereas in reality ferroelectric transition is governed by domain wall motion, analogous to dislocation motion in solids. It is therefore highly important to explore the energetics and transition pathway of ferroelectric domain wall that are relevant to experimental observation and device characterization. In order to acquire a domain wall configuration, we first construct a supercell of pristine monolayer MX consisting of 24 unit cells repeated along the b (y) axis with ferroelectric polarization along $+x$ direction. We then flip the polarization direction of the first 12 unit cells, forming a supercell that contains two 180° ferroelectric domain walls: one at the center ($y = b/2$) and the other at the boundary ($y = 0$). Such configuration obviously satisfies the periodic boundary condition required by first-principles DFT using plane wave basis.

An example of 180° ferroelectric domain wall in monolayer GeS is shown in figure 4(a) with its polarization direction indicated by blue and purple arrows. The domain wall energies were then calculated by the energy difference between the fully relaxed supercell and pristine monolayer MX, which yield 116, 56, 24, and 8 meV Å^{-1} for GeS, GeSe, SnS, and SnSe, respectively. They correspond to effective domain wall energies of 186, 90, 38, and 13 mJ m^{-2} if we assume a vdW thickness of 1 nm. The effective domain wall energies in monolayer GeS and GeSe are similar to the 180° ferroelectric domain wall energies in prototypic $PbTiO_3$ of 132 and 169 mJ m^{-2} for Pb-centered and Ti-centered domain wall, respectively, while SnS and SnSe have the domain wall energies that are similar to $BaTiO_3$ with 7.5 and 16.8 mJ m^{-2} for Ba-centered and Ti-centered domain wall, respectively [46].

We then investigate the energy barrier of 180° ferroelectric domain wall migrating along the $+y$ direction using first-principles NEB method. Here we focus on monolayer GeS. Its final configuration is obtained by translating the supercell of the initial configuration by one lattice vector along the $+y$ axis. Total nine images including the initial and final configurations as well as the linearly interpolated intermediate ones were used in the subsequent NEB calculation. The corresponding MEP is shown in figure 4(b) with the images labeled by 1 to 9. The MEP plot reveals two similar barriers of ~1.6 meV Å^{-1}, owing to the fact that the two Ge-S pairs in a single unit cell are related by translational symmetry along the diagonal direction. The resulted three configurations (#1, #5, and #9) with the same lowest energy are shown in supplementary figure S3, where the corresponding domain wall position is marked by dashed line in each configuration. It is important to notice that the migration barrier of

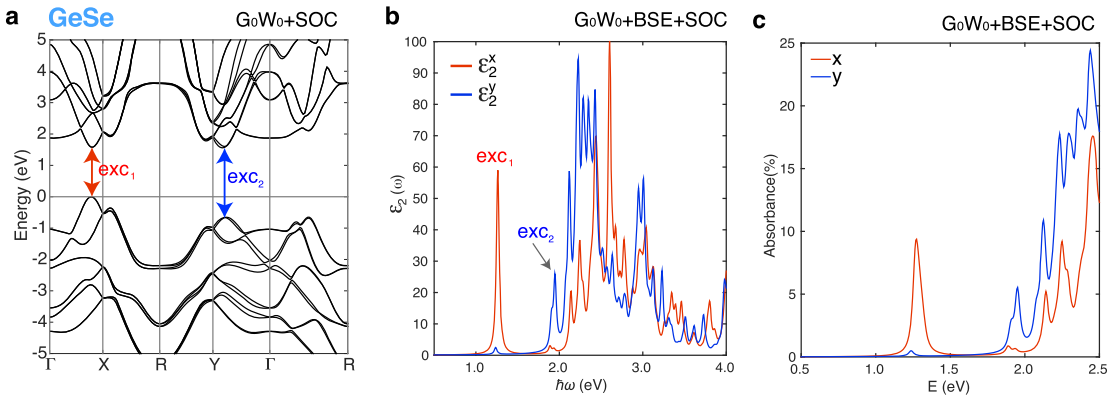

Figure 5. Electronic structure of monolayer GeSe. (a) Band structure of pristine monolayer GeSe. (b) Imaginary dielectric function along the *x* (red) and *y* (blue) direction. Two arrows in the band structure (a) indicate the quasiparticle gap that corresponds to two excitonic peaks in the imaginary dielectric function (b). (c) Absorbance (%) of monolayer GeSe.

~1.6 meV Å^{-1} is remarkably small, which implies that the ferroelectric domain wall in monolayer GeS is highly mobile. Once nucleated, domain wall assisted switching can proceed very fast. We have also calculated MEPs for the other three MX monolayers which are much smaller than that of GeS, indicating that their domain wall motion can be even much faster. It is worth to mention that we also investigated the 90° domain wall, however, the supercell eventually relaxed back to single ferroelectric phase due to the large elastic strain energy residing in the supercell. Hence, it is more likely to observe the 180° domain wall discussed above.

In paraelectric phase, Ge and S of each local pair exactly overlap on the *x*-*y* plane, while in the ferroelectric phase they are shifted with respect to each other. Therefore, one can extract the domain wall width by calculating the relative displacement of each Ge-S local pair in the supercell. Such relative displacement essentially serves as an order parameter which has two components: one along the *x* direction, and the other along the y direction. Figure 4(c) shows the corresponding *x* component of relative displacement as a function of the centers of each Ge-S pair, while the *y* component is presented in supplementary figure S3. Thus, according to figure 4(c), the domain wall width of monolayer GeS is about 1 nm which remains almost unchanged for all nine images in the MEP. By comparing the relative M-X displacement for all four materials (supplementary figure S4), we find that GeS has the smallest domain wall width and the largest relative M-X displacement, followed by GeSe, SnS, and SnSe with gradually increased width and reduced displacement, which is consistent with their ground state structure where GeS has the highest spontaneous strain.

The 180° ferroelectric domain wall in monolayer MX is essentially a one-dimensional interface between two ferroelectric phases with antiparallel electric polarizations. It is inevitably accompanied by distinct electronic structure localized in the vicinity of the domain wall, which is worth of a detailed study. Figure 4(d) presents the DFT-PBE band structure of monolayer GeS supercell with 180° ferroelectric domain wall, where different colors indicate the relative localization of electronic states around the domain wall: purple for the states near the domain wall, and cyan for the states away from the domain wall. It clearly shows that the four lowest conduction bands (from the conduction band minimum (CBM) to CBM + 3) reside near the domain wall, forming two sets of degenerate bands, i.e. degenerate CBM and CBM + 1, and degenerate CBM + 2 and CBM + 3. Figure 4(e) shows the corresponding real-space wavefunctions for CBM at Γ point, while the wavefunction at CBM+2 can be found in supplementary figure S5. The localized electronic wavefunctions positioned at the low energy conduction bands suggest that they may be easily detected via electronic and optical measurement, for examples, by scanning tunneling microscopy and photoluminescence measurement.

5. Electronic structure of ferroelectric monolayer MX

The ferroelectricity and ferroelasticity of monolayer MX discussed above will have more profound impact if they are also coupled to their electronic and optical properties. Figure 5(a) and supplementary figure S6 show the calculated quasiparticle band structure of MX monolayers where both spin-orbit coupling and quasiparticle effect are included. The quasiparticle effect was taken care by many-body perturbation theory within the G_0W_0 approximation [47, 48]. The results demonstrate that MX monolayers are intrinsically 2D semiconducting materials with indirect band gaps ranging from 2.6 eV to 1.1 eV. We also calculated their photoabsorption spectra by solving two-particle Bethe-Salpeter equation [49, 50] based on the quasiparticle energies and the screened Coulomb interactions obtained from the GW calculations. The

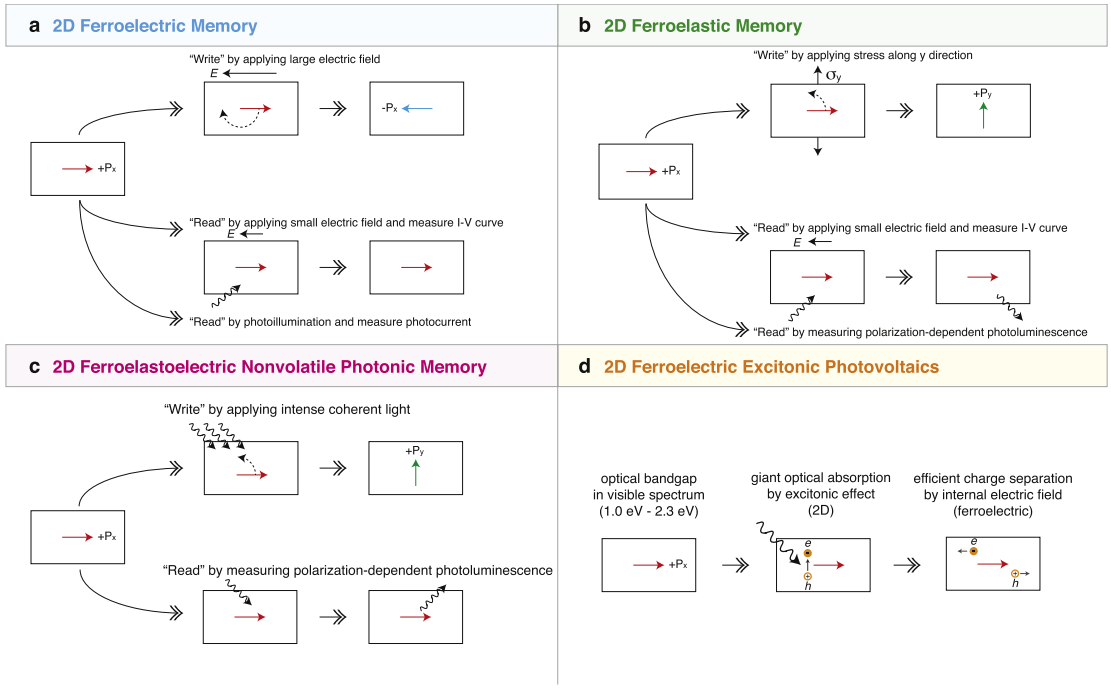

Figure 6. Mechano-opto-electronic device concepts and their mechanisms. (a) 2D ferroelectric memory. (b) 2D ferroelastic memory. (c) 2D ferroelastoelectric nonvolatile photonic memory. (d) 2D ferroelectric excitonic photovoltaics.

calculated lowest exciton energies are 2.3, 1.2, 1.8, 1.0 eV for GeS, GeSe, SnS, and SnSe, respectively, whereas their corresponding direct quasiparticle transition energies are 2.9, 1.6, 2.3, and 1.3 eV, resulting in large exciton binding energies of 0.6, 0.4, 0.5, and 0.3 eV that are similar to monolayer MoS_2 *etc* [44]. In general, the dimensionality reduction leads to a reduced screening in 2D semiconductors, and consequently the effective Coulomb interaction of electron-hole pair becomes much stronger, hence large exciton binding energies in 2D semiconductors are expected upon photoexcitation. Figure 5(b) presents the calculated imaginary dielectric functions with both excitonic and spin-orbit coupling effect included. It illustrates a highly anisotropic photoabsorption in monolayer GeSe with two giant low-energy excitonic peaks: one at 1.2 eV for the *xx* component and the other at 1.9 eV for the *yy* component of the dielectric tensor. Figure 5(c) shows the calculated optical absorbance in percentage [51]. It reveals a strong excitonic optical absorption by monolayer GeSe of 9.4% at 1.3 eV and 5.5% at 2.0 eV corresponding to exciton #1 and #2, respectively. Our results on excitonic behaviors and strong optical absorption agree well with two recent theoretical works [33, 34]. Similar behaviors are found in the other three materials (supplementary figures S7 and S9). Such anisotropic electronic and optical properties are the direct consequences of broken crystalline symmetry due to the ferroelastic spontaneous strain and ferroelectric spontaneous polarization in MX monolayers.

6. Device concepts based on 2D multiferroic monolayer MX

The coupled ferroelastic and ferroelectric orders and the polarization-dependent optical properties within the visible range imply their great potentials for 2D mechano-opto-electronic device applications by manipulating electrical, mechanical, and optical external fields to control the internal responses. For example, as shown in figure 6(a), by applying large external electric field or bias voltage one can switch the polarization direction along the same axis, and by measuring the current-voltage curve under small bias one can detect the state without any detrimental effect, thus implementing the 'write' and 'read' functions of 2*D ferroelectric memory*. The corresponding state can also be detected or 'read' by measuring the photocurrent upon photo-illumination since the internal electric field will determine the drifting directions of photoexcited charge carriers. Furthermore, owing to their ferroelastic nature, applied mechanical stress can also control the polarization state along different in-plane axes (figure 6(b)), which can be 'read' by electrical measurement or by polarization-dependent photoluminescence measurement, rendering a 2*D ferroelastic memory*. Going one step further, one may apply intense coherent light to switch ('write') between the two ferroelastic states through optically-controlled domain wall motion [52], and 'read' out the states through the polarization-dependent photoluminescence measurement, enabling a 2*D ferroelastoelectric non-volatile photonic memory* (figure 6(c)).

Remarkably, this optical induced domain wall motion has been observed very recently by Rubio-Marcos *et al* in $BaTiO_3$ single crystal [50]. Although the present material is different from $BaTiO_3$, it is plausible to observe the similar phenomena in MX monolayers due to the following reasons. First, the domain wall in $BaTiO_3$ possesses two-dimensional nature, while it is 1D in MX monolayers. This means, the optical power needed to initiate the domain wall and flip the ferroelectric polarization will be proportional to domain wall length in MX monolayers, while it is proportional to domain wall area in $BaTiO_3$, thus the scaling for ferroelectric transition is more preferable in 2D MX monolayers. Second, the calculated domain wall energy and migration barrier show large variations among different MX monolayers, thus it offers a wide range of materials choices to achieve optical induced transition with less power. It is important to point out that SnTe, a cousin of the present four MX monolayers, has been synthesized and demonstrated with 2D ferroelectricity very recently by Chang *et al* [53]. Thus the present device proposal can be tested in 2D SnTe. Finally, as shown in figure 6(d), MX monolayers may serve as an ideal materials platform for realizing 2*D ferroelectric photovoltaics*, because (*i*) their optical bandgap falls within the visible range from 1.0 eV to 2.3 eV; (*ii*) their optical absorption is strong due to the pronounced excitonic effect commonly shared by two-dimensional semiconducting materials (figures 5(b) and (c), where monolayer GeSe can absorb more than 6% upon photo-illumination); and (*iii*) the internal in-plane electric field in ferroelectric MX can greatly enhance the separation of the photo-excited charge carriers to form photocurrent. However, we would like to emphasize that all these exciting proposals are at their conceptual stage, and experimental demonstrations have to be carried out in future to validate these concepts in these monolayer MXs.

It is worth to emphasize that the ultrathin two-dimensional nature has another significant implication, that is, the required energy consumption for the 'write' and 'read' operations in the above 2D ferroelectric/ferroelastic/photonic memory will be much smaller than that in thick films. Since the kinetic barrier of the domain wall motion which controls the switching process is small, the operational speed should be very fast. In addition, the non-volatile photonic memory proposed here is based on the ferroelastic transition between two symmetrically-equivalent crystalline states, which is distinct from the recently-demonstrated first photonic switch based on photo-induced crystalline-to-amorphous phase transition [55]. It is worth to mention that, upon the completion of this work, we learned of a few independent works including an experimental study of ferroelectricity in 2D SnTe by Chang *et al* [53] and theoretical studies of MX materials by Wu *et al* [35] and by Mehboudi *et al* [38, 55].

7. Conclusions

To summarize, in this work we discussed both ferroelasticity and ferroelectricity as well as the electronic, optical, and domain wall properties of monolayer group IV monochalcogenides. Monolayer MX represents a class of 2D multiferroic semiconductor with large in-plane spontaneous polarization, spontaneous lattice strain, and small domain wall energy, an important addition to the existing realm of multiferroic bulk materials, interface structures, and thin films. The calculated energy barriers of coherent ferroelectric-to-paraelectric and ferroelastic-to-paraelastic transitions show that their dual ferroic orders are thermodynamically stable at room temperature. In addition, the ferroelectric polarization and coherent transition barrier can be easily tuned via elastic strain engineering. The in-plane ferroelectric polarization in 2D MX monolayers makes them distinctly different from ferroelectric thin-films such as perovskite compounds with out-of-plane polarization whose thickness is intrinsically limited by the amplified out-of-plane depolarization effect [30]. Conversely, a minimal in-plane feature size is expected in MX monolayers due to in-plane depolarization. The strongly-coupled ferroelastic and ferroelectric orders and the polarization-dependent excitonic absorption and photoluminescence within the visible spectrum may enable potential applications for 2D mechano-optoelectronic applications such as 2D ferroelectric excitonic photovoltaics and 2D memory devices including ferroelectric, ferroelastic, and ferroelastoelectric non-volatile photonic memory. The present findings will open up new avenues for miniaturized low-power optoelectronic and photonic applications of 2D multiferroic materials with coupled electronic, optical, mechanical, and even magnetic properties if the symmetry-breaking induced valley-dependent polarization is also considered.

Acknowledgments

H W and X Q acknowledge the start-up funds from Texas A&M University and the computational resources provided by Texas A&M High Performance Research Computing.

Appendix A. Computational details

Atomistic and electronic structures of monolayer group IV monochalcogenides were calculated using first-principles density-functional theory (DFT) [31, 32] as implemented in the Vienna Ab initio Simulation Package (VASP) [56, 57]. We used the Perdew-Burke-Ernzerhof (PBE) [58] form of exchange-correlation functional within the generalized gradient approximation [59, 60], plane wave basis with a cutoff energy of 400 eV, and a Monkhorst-Pack

[61] ***k***-point sampling grid of 10 × 10 × 1. Ground state structures of monolayer group IV monochalcogenides were obtained by fully relaxing both atomic positions and in-plane lattice parameters while keeping a large vacuum region along the plane normal to avoid the periodic image interactions. The maximal residual forces for structural relaxation were less than 0.005 eV $Å^{-1}$, and the convergence criteria for electronic relaxation is 10^{-6} eV. Ferroelectric spontaneous polarization was calculated using the Berry phase approach [39, 40], in which both electronic and ionic contributions were taken into account.

To achieve the minimum energy pathways (MEP) of the coherent ferroelastic and ferroelectric transitions as well as the domain wall migration, we adopted the climbing image nudged elastic band method (CI-NEB) [36] based on the interatomic forces and total energy acquired from the DFT calculations.

Quasiparticle band structures were calculated by many-body perturbation theory calculations within the G_0W_0 approximation [47, 48]. As excitons are expected in 2D semiconductors due to the reduced Coulomb screening, we calculated their dielectric functions and optical absorption spectra by solving two-particle Bethe-Salpeter equation (BSE) [49, 50] using the quasiparticle energies, wavefunctions, and screened Coulomb interactions from the G_0W_0 calculations. Spin-orbit coupling was included in both G_0W_0 and BSE calculations.

References

[1] Novoselov K S, Jiang D, Schedin F, Booth T J, Khotkevich V V, Morozov S V and Geim A K 2005 *Proc. Natl Acad. Sci. USA* **102** 10451

[2] Novoselov K S, Geim A K, Morozov S V, Jiang D, Zhang Y, Dubonos S V, Grigorieva I V and Firsov A A 2004 *Science* **306** 666

[3] Novoselov K S, Geim A K, Morozov S V, Jiang D, Katsnelson M I, Grigorieva I V, Dubonos S V and Firsov A A 2005 *Nature* **438** 197

[4] Wang Q H, Kalantar-Zadeh K, Kis A, Coleman J N and Strano M S 2012 *Nat. Nanotech.* **7** 699

[5] Geim A K and Grigorieva I V 2013 *Nature* **499** 419

[6] Butler S Z *et al* 2013 *ACS Nano* **7** 2898

[7] Andor K, Guido B, Martin G, Jaroslav F, Viktor Z, Neil D D and Vladimir F K 2015 *2D Mater.* **2** 022001

[8] Hasan M Z and Kane C L 2010 *Rev. Mod. Phys.* **82** 3045

[9] Qi X-L and Zhang S-C 2011 *Rev. Mod. Phys.* **83** 1057

[10] Qi J, Qian X, Qi L, Feng J, Shi D and Li J 2012 *Nano Lett.* **12** 1224

[11] Duerloo K-A N, Ong M T and Reed E J 2012 *J. Phys. Chem. Lett.* **3** 2871

[12] Wu W *et al* 2014 *Nature* **514** 470

[13] Zhu H, Wang Y, Xiao J, Liu M, Xiong S, Wong Z J, Ye Z, Ye Y, Yin X and Zhang X 2015 *Nat. Nanotech.* **10** 151

[14] Fei R, Li W, Li J and Yang L 2015 *Appl. Phys. Lett.* **107** 173104

[15] Gomes L C, Carvalho A and Neto A C 2015 *Phys. Rev.* B **92** 214103

[16] Li X and Yang J 2014 *J Mater. Chem.* C **2** 7071

[17] Blonsky M N, Zhuang H L, Singh A K and Hennig R G 2015 *ACS Nano* **9** 9885

[18] Lin M-W *et al* 2016 *J. Mater. Chem.* C **4** 315

[19] Qian X, Liu J W, Fu L and Li J 2014 *Science* **346** 1344

[20] Liu J, Wang H, Fang C, Fu L and Qian X 2016 *Nano Lett.* in press (doi:10.1021/acs.nanolett.6b04487)

[21] Li W and Li J 2016 *Nat. Commun.* **7** 10843

[22] Qian X, Wang Y, Li W, Lu J and Li J 2015 *2D Mater.* **2** 032003

[23] Hill N A 2000 *J. Phys. Chem.* B **104** 6694

[24] Wang J *et al* 2003 *Science* **299** 1719

[25] Eerenstein W, Mathur N and Scott J F 2006 *Nature* **442** 759

[26] Cheong S-W and Mostovoy M 2007 *Nat. Mater.* **6** 13

[27] Ramesh R and Spaldin N A 2007 *Nat. Mater.* **6** 21

[28] Picozzi S and Ederer C 2009 *J. Phys. Condens. Matter* **21** 303201

[29] Beckman S, Wang X, Rabe K M and Vanderbilt D 2009 *Phys. Rev.* B **79** 144124

[30] Ahn C, Rabe K and Triscone J-M 2004 *Science* **303** 488

[31] Hohenberg P and Kohn W 1964 *Phys. Rev.* B **136** B864

[32] Kohn W and Sham L J 1965 *Phys. Rev.* **140** A1133

[33] Gomes L C and Carvalho A 2015 *Phys. Rev.* B **92** 085406

[34] Shi G and Kioupakis E 2015 *Nano Lett.* **15** 6926

[35] Wu M and Zeng X C 2016 *Nano Lett.* **16** 3236

[36] Henkelman G, Uberuaga B P and Jónsson H 2000 *J. Chem. Phys.* **113** 9901

[37] Sheppard D, Xiao P, Chemelewski W, Johnson D D and Henkelman G 2012 *J. Chem. Phys.* **136** 074103

[38] Mehboudi M *et al* 2016 *Nano Lett.* **16** 1704

[39] King-Smith R and Vanderbilt D 1993 *Phys. Rev.* B **47** 1651

[40] Resta R 1994 *Rev. Mod. Phys.* **66** 899

[41] Fei R, Kang W and Yang L 2016 *Phys. Rev. Lett.* **117** 097601

[42] Devonshire A F 1949 *Philos. Mag.* **40** 1040

[43] Bertolazzi S, Brivio J and Kis A 2011 *ACS Nano* **5** 9703

[44] Feng J, Qian X, Huang C-W and Li J 2012 *Nat. Photon.* **6** 866

[45] Chen L-Q 2008 *J. Am. Ceram. Soc.* **91** 1835

[46] Meyer B and Vanderbilt D 2002 *Phys. Rev.* B **65** 104111

[47] Hedin L 1965 *Phys. Rev.* **139** A796

[48] Shishkin M and Kresse G 2006 *Phys. Rev.* B **74** 035101

[49] Salpeter E E and Bethe H A 1951 *Phys. Rev.* **84** 1232

[50] Onida G, Reining L and Rubio A 2002 *Rev. Mod. Phys.* **74** 601

[51] Fox M 2010 *Optical Properties of Solids* (Oxford: Oxford University Press)

[52] Rubio-Marcos F, Del Campo A, Marchet P and Fernández J F 2015 *Nat. Commun.* **6**

[53] Chang K *et al* 2016 *Science* **353** 274

[54] Mehboudi M *et al* 2016 *Phys. Rev. Lett.* **117** 246802

[55] Ríos C, Stegmaier M, Hosseini P, Wang D, Scherer T, Wright C D, Bhaskaran H and Pernice W H P 2015 *Nat. Photon.* **9** 725

[56] Kresse G and Hafner J 1993 *Phys. Rev.* B **47** 558

[57] Kresse G and Furthmüller J 1996 *Comput. Mater. Sci.* **6** 15

[58] Perdew J P, Burke K and Ernzerhof M 1996 *Phys. Rev. Lett.* **77** 3865

[59] Becke A D 1988 *Phys. Rev.* A **38** 3098

[60] Langreth D C and Mehl M J 1983 *Phys. Rev.* B **28** 1809

[61] Monkhorst H J and Pack J D 1976 *Phys. Rev.* B **13** 5188